Article

Utilizing Machine Learning and Diode Physics to Investigate the Effects of Stoichiometry on Photovoltaic Performance in Sequentially Processed Perovskite Solar Cells

Jeongbeom Cha, Dohun Baek, Haedam Jin, Hyemi Na, Geon Yeong Park, Dong Seok Ham, and Min Kim*

Read Online

ACCESS | Metrics & More | Article Recommendations | SI Supporting Information

ABSTRACT: Organic−inorganic metal halide perovskite solar cells are renowned for their extensive solution processability, although the production of uniformly crystalline perovskite films can necessitate intricate deposition methods. In our study, we harmonized Shockley diode-based numerical analysis with machine learning techniques to extract the device characteristics of perovskite solar cells and optimize their photovoltaic performance in light of the experimental variables. The application of the Shockley diode equation facilitated the extraction of photovoltaic parameters and the prediction of power conversion efficiencies, thus aiding the understanding of device physics and charge recombination. Through machine learning, specifically Gaussian process regression, we trained models on current−voltage curves sensitive to variations in fabrication conditions, thereby pinpointing the optimal settings for enhanced device performance. Our multifaceted approach not only clarifies the interplay between experimental conditions and device performance but also streamlines the optimization process, diminishing the need for exhaustive trial-and-error experiments. This methodology holds substantial promise for advancing the development and fine-tuning of next-generation perovskite solar cells.
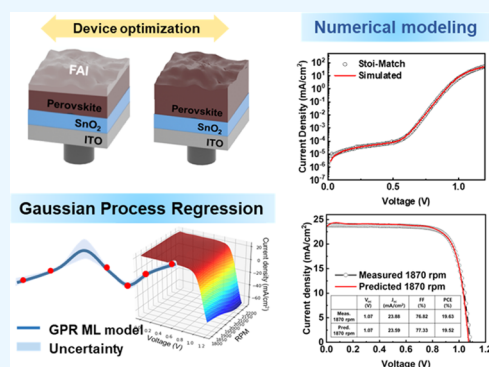
1. INTRODUCTION

Organic−inorganic perovskite photovoltaics are considered the next-generation solar cells due to their rapid increase in power conversion efficiency (PCE), reaching over 25.7%, and their low-cost solution-based processing methods.[1−3] The most widely used perovskite structure, ABX_3, is composed of formamidinium iodide (FAI) and lead iodide (PbI_2) and is processed using solution-based perovskite conversion methods such as the antisolvent quenching one-step method and the sequential deposition two-step method.[4,5] The one-step deposition method allows for easy control of the perovskite film stoichiometry by changing the molar ratio of PbI_2 and organic salts (FAI, MAI, and MABr) in the perovskite precursor solution. However, controlling the antisolvent quenching treatment during the spin-casting of the perovskite solution can be difficult, leading to kinetically frozen perovskite phases and increased complexity and variability in device performance. Additionally, antisolvents used for perovskite conversion, such as chlorobenzene, toluene, and diethyl ether, are known to be environmentally toxic.[6]

The sequential deposition method involves separate coating processes for PbI_2 and FAI layers, which are converted to perovskite films through ion diffusion during thermal annealing. Compared to the one-step deposition method, the sequential deposition method produces thermodynamically stable perovskite crystals, resulting in high-quality perovskite films with high reproducibility. This advantage makes the method more suitable for large-area coatings, such as roll-to-roll and spray coating.[7−10] However, a disadvantage of the sequential deposition method is the difficulty in accurately determining the stoichiometric ratio of the perovskite film, as the relative molar quantity of each component cannot be precisely controlled by the thickness of each layer. Consequently, depending on the processing parameters, the two-step procedure can cause excess PbI_2 (Ex-PbI_2) and excess FAI (Ex-FAI) on the perovskite surface,[10] which may also induce the formation of trap states and act as a charge-blocking layer between the perovskite layer and charge transport layer.[11,12]

To address the stoichiometric challenges in the sequential deposition method, several studies have been conducted to optimize deposition parameters such as PbI_2 and FAI solution concentrations, spin-coating speeds, and annealing temper-
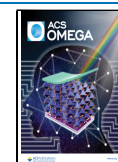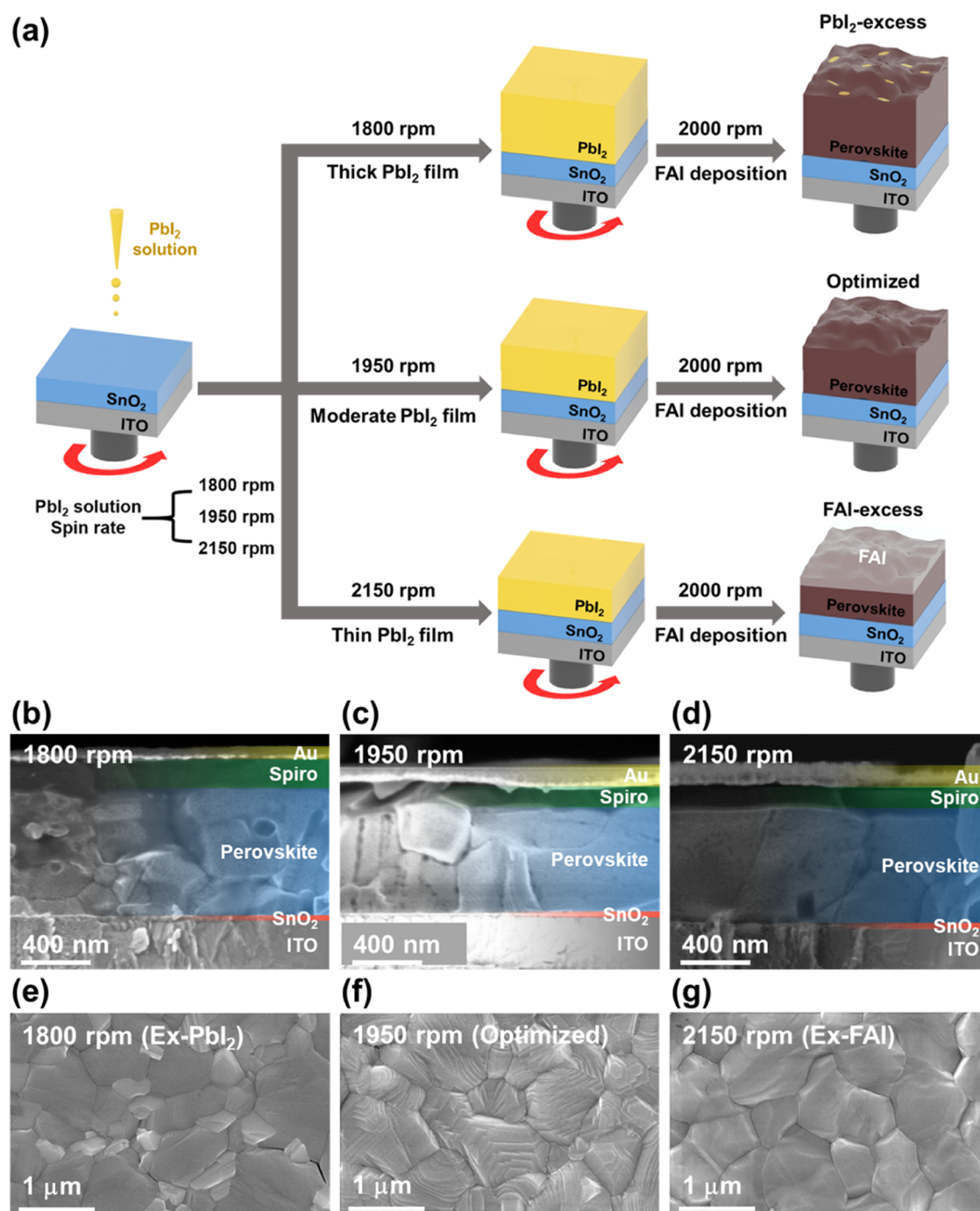
Figure 1. (a) Schematic of the device fabrication for different PbI$_2$ rpms (1800, 1950, and 2150 rpm). Cross-sectional SEM images of the perovskite layer processed from PbI$_2$ at (b) 1800, (c) 1950, and (d) 2150 rpm. SEM images of the perovskite layer processed from PbI$_2$ at (e) 1800, (f) 1950, and (g) 2150 rpm.

atures.[13,14] However, most of these studies have relied on trial-and-error approaches, which are time-consuming and resource intensive. Recently, machine learning techniques have emerged as powerful tools for optimizing complex experimental parameters and predicting material properties, enabling the more efficient exploration of parameter spaces. By integrating experimental data with machine learning models, researchers can rapidly identify optimal processing conditions for perovskite solar cells, thereby improving their performance and reproducibility.

In this study, we propose a synergistic approach that integrates the Shockley diode equation with machine learning techniques to optimize sequentially processed perovskite solar cells. First, we use a numerical method for fitting that allows us to extract device characteristics of stoichiometrically modified perovskite solar cells. This diode-equation-based fitting provides a comprehensive understanding of how stoichiometry influences device performance and charge recombination within these solar cells. Second, we apply Gaussian process regression to directly train $J-V$ curves of the perovskite devices under various experimental conditions, facilitating predictions
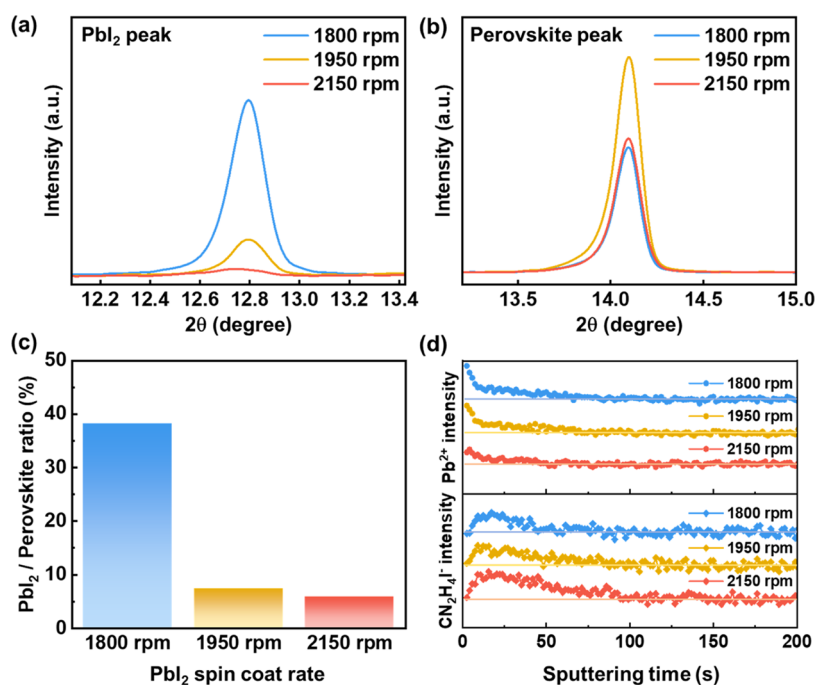
Figure 2. XRD patterns of the perovskite layer for the (a) PbI_2 peak and (b) perovskite peak, depending on PbI_2 (1800, 1950, and 2150 rpm). (c) Intensity ratio of perovskite to PbI_2 XRD peaks. (d) TOF-SIMS profiles of the perovskite layer for Pb^{2+} and $CN_2H_4I^-$.

of $J-V$ curves in unexplored parameter spaces and identification of optimal conditions. Our research demonstrates the potential of machine learning-assisted optimization in developing high-performance optoelectronic devices, thus significantly contributing to the evolution of perovskite solar cell technology.

2. RESULTS AND DISCUSSION

2.1. Stoichiometric Variations of Sequentially Processed Perovskite Films. We adopted the sequential deposition process of the perovskite film (FAP-bI$_3$)$_{0.97}$(MAPbBr$_3$)$_{0.03}$, which involves the spin-coating of PbI_2 and organic salts in a layer-by-layer manner. Considering that 97% of the organic cations are FA^+ ions, the organic salt layer was designated FAI as a representative. To deviate the relative compositional ratio of PbI_2 and FAI from that of the $FAPbI_3$ structure, the thickness of the PbI_2 and FAI layers can be controlled by varying the spin-coating parameters, such as the spinning rate, concentration, and solvent viscosity.[15,16] In this study, we controlled the spin-coating rate of the PbI_2 layer from 1800 to 2150 rpm while fixing the spin-coating rate of the FAI layer at 2000 rpm. The lower the spin-coating rate, the thicker the resulting film. Therefore, by simply controlling the spin-coating rate of PbI_2, we can control the relative composition ratio of the perovskite components, resulting in excess-PbI_2, excess-FAI, and optimized perovskite phases. We chose three rpm parameters: 1800 rpm for the thick PbI_2 film (resulting in PbI_2-excess perovskite, briefly Ex-PbI_2), 1950 rpm for the moderate PbI_2 film (Optimized), and 2150 rpm for the thin PbI_2 film (FAI-excess perovskite, briefly Ex-FAI) (Figure 1a).

Cross-sectional scanning electron microscopy (SEM) images were obtained to characterize the thickness of the perovskite films. Most of the fabricated high-performance PSCs have perovskite film thicknesses of approximately 500−700 nm.[17,18] The thickness of the perovskite film processed from the 1800-rpm PbI_2 film was approximately 600 nm (Figure 1b), and the thickness of the perovskite films processed from 1950- and 2150 rpm PbI_2 films was 500−550 nm (Figure 1c,d). Top-view SEM images were obtained to observe the morphologies of the perovskite films. All the perovskite films had similar grain sizes of 0.8 to 1 μm. PbI_2 crystals (bright color) were observed among the perovskite grains in the perovskite film coated at 1800 rpm (Figure 1e). On the 1950 rpm, the SEM image shows a few PbI_2 crystals on the surface of the perovskite film, and a clear pattern of perovskite crystals was observed (Figure 1f). Similarly, the 2150 rpm SEM image has few PbI_2 crystals; however, the pattern of perovskite crystals is not observed clearly because the perovskite grains are covered by excess-FAI (Figure 1g). PbI_2-excess perovskite exhibits a higher surface roughness than the 1950 rpm and FAI-excess perovskite films owing to the spiky formation of PbI_2 crystals (Figure S1).

Crystal structure and elemental analyses were carried out to confirm the optimization of the PbI_2/FAI stoichiometry. X-ray diffraction (XRD) measurements were conducted to quantify the relative amount of PbI_2 crystals and the crystallinity of the perovskite films. The diffraction peak intensity designated to the PbI_2 crystal (12.8°) also decreased with decreasing thickness of the PbI_2 layer and a spin rate from 1800 to 2150 rpm (Figure 2a). In the case of perovskite processed from 2150 rpm PbI_2, the PbI_2 diffraction peak disappears, indicating that the PbI_2 phase is completely converted into the perovskite phase. The (100) crystalline peak of the perovskite was compared, which showed an increase only when the perovskite was processed from the 1950 rpm PbI_2 layer (Figure 2b). We also calculated the ratio of PbI_2 to perovskite peak intensity (Figure 2c). The intensity ratio of the perovskite to PbI_2 XRD peaks is 38.21% at 1800 rpm, 7.32% at 1950 rpm, and 5.84% at 2150 rpm, which indicates that the amount of excess-PbI_2 is reduced with a decreasing thickness of the PbI_2 layer.

Additionally, we analyzed the depth profile of each perovskite film using time-of-flight secondary ion mass

Table 1. Average and Champion Device's Photovoltaic Parameters of Perovskite Solar Cells for 1800 rpm (Ex-PbI$_2$), 1950 rpm (Optimized), and 2150 rpm (Ex-FAI)[a]

		V_{oc} (V)	J_{sc} (mA/cm^2)	FF (%)	PCE (%)	H_{index} (%)
1800 rpm (Ex-PbI$_2$)	average	1.01 ($\pm$0.02)	23.40 ($\pm$0.10)	76.55 ($\pm$1.98)	18.12 ($\pm$0.44)	2.41
	champion	1.05	23.46	78.22	19.27	
1950 rpm (optimized)	average	1.06 ($\pm$0.03)	23.47 ($\pm$0.29)	77.62 ($\pm$1.61)	19.16 ($\pm$0.53)	3.96
	champion	1.10	23.84	78.32	20.54	
2150 rpm (Ex-FAI)	average	0.96 ($\pm$0.04)	22.92 ($\pm$0.24)	73.92 ($\pm$1.15)	16.05 ($\pm$0.65)	6.59
	champion	1.03	23.23	76.48	18.30	

[a]H_{index} (%) = (PCE$_{reverse}$ − PCE$_{forward}$)/PCE$_{reverse}$ × 100.
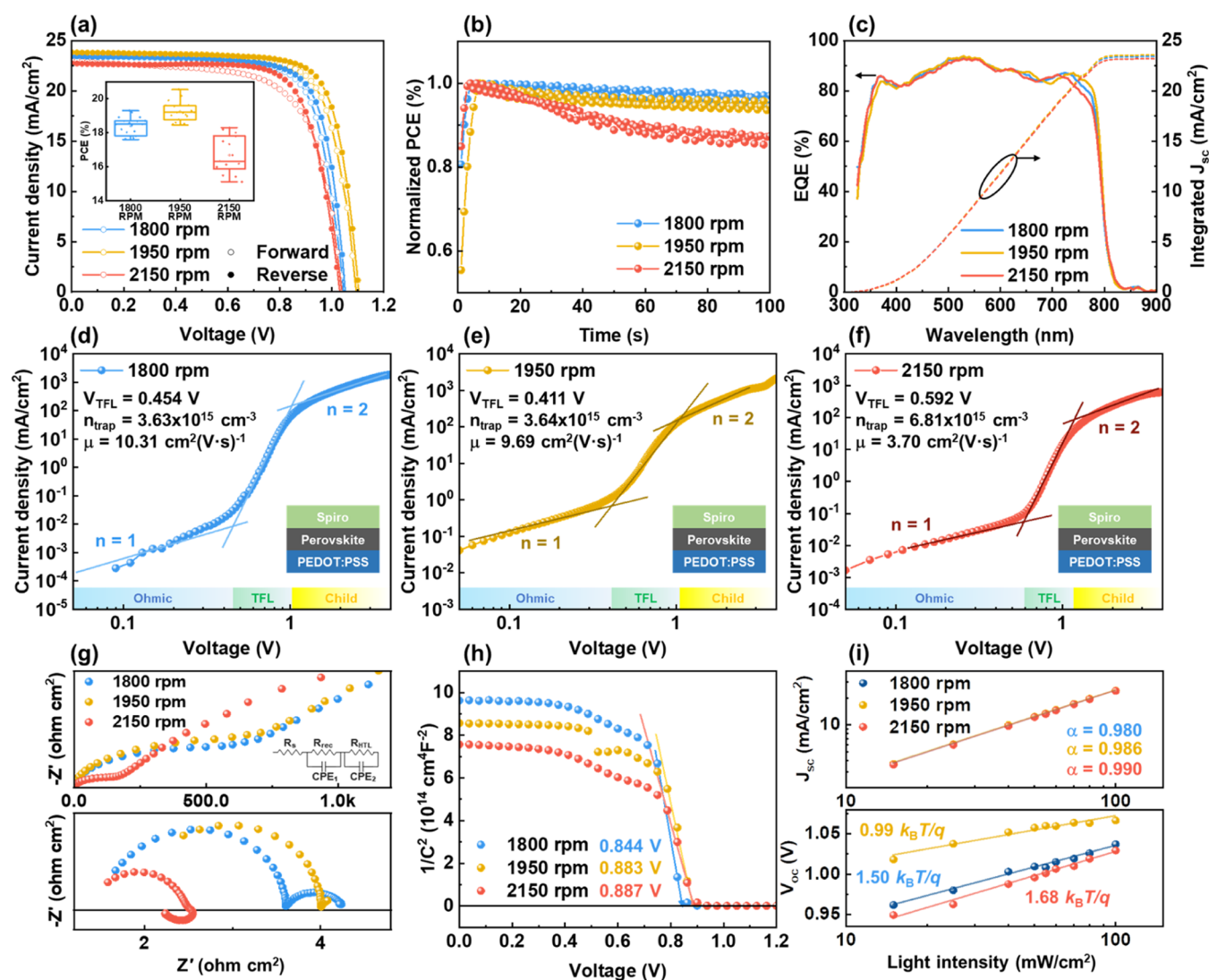

Figure 3. (a) Forward and reverse photo $J−V$ characteristics of the devices. The inset shows the PCE histogram for different PbI$_2$ spin-coating rates. (b) Normalized PCE curves of the devices obtained from maximum power point (MPP) tracking measurement. (c) EQE and integrated J_{sc} spectra of the devices. Space-charge-limited current (SCLC) measurement of hole-only devices processed from (d) 1800, (e) 1950, and (f) 2150 rpm. (g) Nyquist plot of the devices measured under dark (top) and 1 sun illumination (bottom). (h) Mott−Schottky plot. (i) Light intensity-dependent J_{sc}, V_{oc}, and ideality factor of the devices.

spectrometry (TOF-SIMS) (Figure 2d). In these profiles, Pb^{2+} ions were chosen to represent both PbI$_2$ and the bulk perovskite, while CN$_2$H$_4$I$^−$ ions were selected as representatives for FAI, in accordance with the prior literature.[19] We introduced a baseline on the graph to highlight the stabilized signals of Pb^{2+} and CN$_2$H$_4$I$^−$ within the bulk of the perovskite film, enabling a clear contrast between the surface and bulk ion intensities. Corroborating the findings from our XRD

measurements, the intensity of the Pb^{2+} signal on the perovskite surface decreased with an increasing spin-coating rate of the PbI$_2$ deposition process. Intriguingly, an excess of FAI was detected across all perovskite films, likely due to the sequential deposition method used. However, the film spun at 2150 rpm exhibited the highest surface concentration of FAI.

Through a combination of SEM, XRD, and TOF-SIMS analyses, we confirmed that the perovskite film produced at

1800 rpm had an excess of PbI_2 (Ex-PbI_2), while the film at 2150 rpm was characterized by an excess of FAI (Ex-FAI). The film fabricated at 1950 rpm was identified as the optimized perovskite film, given its relatively lower concentrations of both PbI_2 and FAI compared to those at 1800 and 2150 rpm. This suggests that the individual coated layers of PbI_2 and FAI are efficiently converted to a uniform perovskite film at a spin-coating speed of 1950 rpm.

2.2. Photovoltaic Characteristics of the Perovskite Solar Cells. To thoroughly investigate the photovoltaic characteristics of the processed perovskite solar cells, current density−voltage (J−V), space-charge-limited current (SCLC), and electrochemical impedance spectroscopy (EIS) were performed. The photovoltaic properties of the processed perovskite devices with 1800, 1950, and 2150 rpm are collected under one sun illumination (Table 1). The PCE histogram reveals that 1800 (19.27%) and 2150 (18.30%) rpm decreased the PCE compared to the 1950 rpm devices (20.54%), and 2150 rpm devices have a broad distribution of photovoltaic parameters (Figure 3a). The optimized device achieved an open-circuit voltage (V_{oc}) of 1.10 V, a short-circuit current density (J_{sc}) of 23.84 mA/cm^2, a fill factor (FF) of 78.32%, and a PCE of 20.54%. The 1800 and 2150 rpm devices have lower V_{oc} and J_{sc} values, with the 2150 rpm device having the lowest photovoltaic values (V_{oc} of 1.03 V, J_{sc} of 23.23 mA/cm^2). The reason for this is that the Ex-FAI phase leads to a significant reduction in PCE due to the insulating property of FAI at the device interfaces, as compared to the Ex-PbI_2 p-type semiconductor phase.[20−25] The hysteresis index (H_{index}) was calculated from the difference between the forward and reverse I−V scans, which is related to the charge accumulation between the perovskite layer and charge transport layer.[26−30] As the relative amount of PbI_2 phases decreases, H_{index} continuously increases, which indicates that Ex-PbI_2 phase accelerates carrier extraction and inhibits charge accumulation, in accordance with previous results.[31−34]

Maximum power point (MPP) tracking measurements were conducted to investigate the device's operational stability at the maximum power point under constant illumination of 100 mW/cm^2 for 100 s (Figure 3b). The 1800 and 1950 rpm devices retained over 95% of the initial PCE, whereas it reduced to 85% in 2150 rpm devices. This indicates that Ex-FAI degrades the stability of the device under light and causes charge accumulation, which agrees well with the increase in the hysteresis index.[31−34] EQE spectra were also obtained to calculate the J_{sc} values of the devices (Figure 3c). Although the devices have similar EQE edges, the 1950 rpm device shows the highest integrated J_{sc} of 23.58 mA/cm^2, compared to 1800 rpm (23.42 mA/cm^2) and 2150 rpm (23.21 mA/cm^2). The trends of the integrated J_{sc} from the EQE spectra match well with those of J_{sc} from the photo J−V curves.

We fabricated hole-only devices, ITO/PEDOT: PSS/perovskite/Spiro-OMeTAD, for SCLC measurements to confirm the trap density (n_{trap}) and mobility (μ) of the devices (Figure 3d–3f).[35,36] The equations used for the calculation of trap density and mobility from SCLC measurements are

$$n_{trap} = \frac{2\varepsilon\varepsilon_0 V_{TFL}}{eL^2}$$

(1)

and

$$J_{SCL} = \frac{9\varepsilon\varepsilon_0 \mu V^2}{8L^3}$$

(2)

where ε and ε_0 are the dielectric constants of the perovskite and the vacuum permittivity, respectively, L (600 nm for Ex-PbI_2, 550 nm for 1950 rpm, and 500 nm for Ex-FAI) is the thickness of the obtained perovskite film, e is the elementary charge, and J_{SCL} is the measured current density. The trap-filled limit voltage (V_{TFL}) was 0.454 V for 1800 rpm, 0.411 V for 1950 rpm, and 0.592 V for 2150 rpm. The 2150 rpm device shows the highest trap density of 6.81×10^{15} cm^{-3} compared to 1800 rpm (3.63×10^{15} cm^{-3}) and 1950 rpm (3.64×10^{15} cm^{-3}). The calculated mobility from SCLC measurements is 10.31 cm^2 (V·s)$^{-1}$ for 1800 rpm, 9.69 cm^2 (V·s)$^{-1}$ for 1950 rpm, and 3.70 cm^2 (V·s)$^{-1}$ for 2150 rpm. As the amount of excess-PbI_2 increased from 2150 to 1800 rpm, the mobility also increased. This indicates that excess-PbI_2 induces few trap states and reduces charge accumulation, which agrees with the MPP tracking and a decrease in the hysteresis index.[31−34]

Additionally, we conducted steady-state photoluminescence (PL) measurement on perovskite films processed at 1800, 1950, and 2150 rpm (Figure S4). The film processed at 1950 rpm displayed the highest PL intensity, when compared to those processed at 1800 and 2150 rpm. This suggests that there is reduced nonradiative recombination due to trap states in the 1950 rpm film. Moreover, the PL peak shifts toward longer wavelengths as the spin-coating speed decreases. According to prior studies, an excess of PbI_2 leads to this shift in the PL peak toward longer wavelengths.[37−39] Notably, the PL peak of the 1800 rpm film, which contains the largest amount of PbI_2, appears at the longest wavelength. These observations are entirely consistent with results from SEM, XRD, TOF-SIMS, and SCLC analyses.

Electrochemical impedance spectroscopy analysis was performed to further elucidate carrier transfer and recombination characteristics within the devices. Nyquist plots were acquired over a frequency range of 100 Hz to 1 MHz at a bias of 0.6 V, both under dark conditions and under 1 sun illumination (Figure 3g). As established in previous studies, the series resistance (R_s) can be determined at the point where the Nyquist plot intersects the real axis, and our analysis found no significant difference in R_s among the devices.[40−42] Two distinctive arcs were noticeable in the Nyquist spectra; the one in the high-frequency range corresponds to charge recombination resistance (R_{rec}).[40−42] The spectra, when measured under drak conditions, were fitted to an equivalent circuit model. The device processed at 1800 rpm exhibited a slight decrease in R_{rec}, falling to 583 Ω cm^2. A more pronounced reduction was observed in the device spun at 2150 rpm, with a value of 144 Ω cm^2, in comparison to the 1950 rpm device, which had an R_{rec} of 662 Ω cm^2. Regarding shunt resistance, R_{sh}, values for devices processed at 1800, 1950, and 2150 rpm under 1 sun illumination closely paralleled those obtained under dark conditions, with values of 2.04, 2.14, and 0.96 Ω cm^2, respectively. A reduction in R_{rec} is indicative of increased carrier recombination in PSCs, and higher recombination rates typically result in lower and more variable V_{oc}.[40−42] Additionally, a negative value was noted in the device processed at 2150 rpm when measured under illumination, suggesting charge accumulation at the interface.[43] These results are consistent with our conclusion that the excess FAI impacts charge extraction, as evidenced by the broad distribution of photovoltaic parameters (Figure S3).

Mott−Schottky plots were collected and analyzed to investigate the built-in potential (V_{bi}) based on the following equation[44−46]
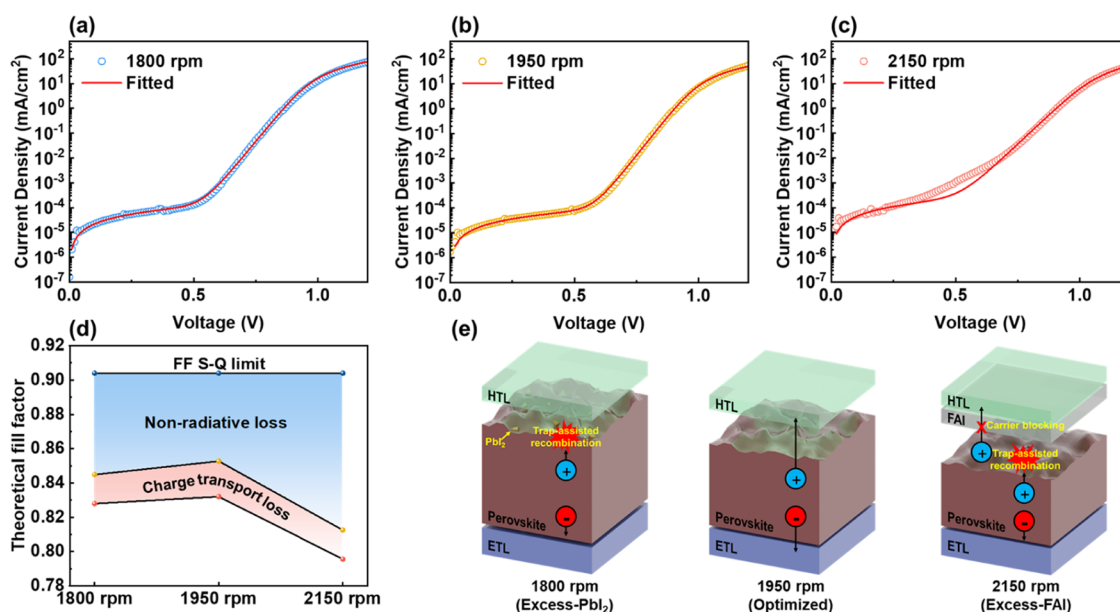
Figure 4. Dark $J-V$ curves of devices and fitted dark $J-V$ curves with the Shockley's diode equation from (a) 1800 rpm (Ex-PbI$_2$), (b) 1950 rpm (optimized), and (c) 2150 rpm (Ex-FAI). (d) Theoretical fill factor of each device calculated by using extracted parameters from fitted dark $J-V$ curves. (e) Schematics of the carrier transport mechanism of the 1800, 1950, and 2150 rpm devices.

$$\frac{1}{C^2} = \frac{2}{q\varepsilon\varepsilon_0 A^2 N}(V_{bi} - V) \tag{3}$$

where C is the capacitance, N the carrier density, ε the static permittivity, and ε_0 the static permittivity. The x-intercept of the Mott−Schottky plot indicates the built-in potential. The 1800 rpm decreases V_{bi} by 0.844 V compared to that of 1950 rpm (0.883 V), which is in accordance with a lower V_{oc} value of the 1800 rpm device than that of the 1950 rpm device (Figure 3h).[47,48] On the other hand, the 2150 rpm device exhibits a higher built-in potential of 0.887 V than the 1950 rpm device, even though the 2150 rpm device has a lower V_{oc} than the 1800 rpm device. This conflicting result can be attributed to the fact that the 2150 rpm device has a high trap density and low shunt resistance, leading to significant nonradiative recombination and leakage current. This stronger recombination and leakage result in a V_{oc} of 2150 rpm that is lower than that of 1800 rpm in photovoltaic devices. Moreover, electron lifetime (τ) was calculated from the Bode plots following the eq (Figure S5)

$$\tau = \frac{1}{2\pi f} \tag{4}$$

where τ is the electron lifetime and f is the peak frequency at the minimum phase angle. The calculated τ values of 1800, 1950, and 2150 rpm are 6.34, 7.98, and 3.18 μs, respectively, and the longer lifetime indicates the reduction of the electron recombination.

To further understand the carrier recombination mechanism in the devices, a light intensity-dependent $J_{sc}-V_{oc}$ plot was obtained. The light intensity-dependent J_{sc} follows the power law ($J_{sc} \propto I^\alpha$): A decrease in the slope indicates bimolecular recombination under short-circuit conditions, and all of the devices have similar values of α (Figure 3i).[49−51] Slope of light intensity-dependent V_{oc} plot was calculated as 1.50 $k_B T/q$ for 1800 rpm, 0.99 $k_B T/q$ for 1950 rpm, and 1.68 $k_B T/q$ for 2150 rpm (Figure 3i). The ideality factor (n_{id}) was also obtained

from the light intensity-dependent $J_{sc}-V_{oc}$ plot based on the following equation

$$V_{oc} = \frac{n_{id} k_B T}{q}\ln\left(\frac{J_{sc}}{J_0}\right) \tag{5}$$

where J_0 is the saturation current density, q is the elementary charge, n_{id} is the ideality factor, k_B is the Boltzmann constant, and T is the absolute temperature. When compared to the 1800 rpm (1.53) and 2150 rpm (1.67) devices, the computed ideality factor of the 1950 rpm device is 1.00, indicating suppression of trap-induced recombination.[52−56]

2.3. Shockley Diode-Based Numerical Analysis of the Perovskite Solar Cells. The multivariable diode model equation was utilized to characterize the relationship between dark J and V of the device. The four photovoltaic parameters (diode saturation current, J_0, ideality factor, n_{id}, shunt, R_{sh}, and series resistance, R_s) were obtained, which were further used for the calculation of theoretical fill factor and power conversion efficiency. For numerical modeling, dark $J-V$ curves of photovoltaic devices without illumination have been studied to characterize diode properties. The dark $J-V$ curves of 1800, 1950, and 2150 rpm were fitted based on the dark $J-V$ curves using the Shockley's diode equation, as follows[57,58]

$$J = J_0\left\{\exp\left[\frac{q}{n_{id} k_B T}(V - JAR_s)\right] - 1\right\} + \frac{V - JAR_s}{AR_{sh}}$$
$$- J_{ph}(V) \tag{6}$$

where J is the current density, J_0 is the dark saturation current density, q is the elementary charge, n_{id} is the ideality factor, k_B is the Boltzmann constant, T is the absolute temperature, A is the active area of the solar cell, R_s is the series resistance, R_{sh} is the shunt resistance, and $J_{ph}(V)$ is the voltage-dependent photogenerated current density (Figure 4a−4c). By fitting the dark $J-V$ curves, we extracted the values of J_0, n_{id}, R_s, and R_{sh} and summarized them (Table 2).

Table 2. Extracted Parameters of 1800 rpm (Ex-PbI$_2$), 1950 rpm (Optimized), and 2150 rpm (Ex-FAI) from the Dark J−V Curve by Using Shockley's Diode Equation (eq 6)

	J_0 (mA/cm^2)	n_{id}	R_s (Ω·cm^2)	R_{sh} (Ω·cm^2)	calc.V_{oc} (V)	meas.V_{oc} (V)
1800 rpm (Ex-PbI$_2$)	4.17×10^{-11}	1.40	2.5	4.58×10^6	0.97	1.01
1950 rpm (optimized)	5.02×10^{-12}	1.35	3.2	6.90×10^6	1.00	1.06
2150 rpm (Ex-FAI)	3.02×10^{-9}	1.79	2.1	2.28×10^6	0.95	0.96

The 1950 rpm device exhibits the lowest value of dark saturation current density, which represents the total of all recombination processes, such as Shockley−Read−Hall (SRH), surface, contact, and Auger recombination mechanisms.[59−62] The ideality factor indicates how closely the device adheres to the diode equation, with radiative recombination being favorable when the value is close to 1.[52−56] Both 1800 and 2150 rpm devices display an increase in the ideality factor, with the 2150 rpm device having the highest n_{id} value of 1.79. These ideality factors are consistent with the calculated n_{id} values from the light intensity-dependent J_{sc}−V_{oc} plot. The increase in J_0 and n_{id} suggests that excess-PbI$_2$ and excess-FAI induce nonradiative recombination.[52−56,59−62]

Although the devices exhibit similar R_s, R_{sh} is reduced in both 1800 and 2150 rpm devices compared to the 1950 rpm device. R_{sh} is mainly affected by defects in the perovskite layer, significantly influencing the solar cell efficiency. Lower R_{sh} results in lower V_{oc} and J_{sc} values for 1800 and 2150 rpm devices compared to the 1950 rpm devices.[63−68] The changes in R_s and R_{sh} for each device are consistent with the results from the Nyquist plot analysis. Moreover, we calculated V_{oc} using the extracted parameters from the dark J−V curve[69,70] based on

$$V_{oc} = \frac{n_{id}k_BT}{q}\ln\left[\frac{J_{ph}(V_{oc})}{J_0} + 1\right] \quad (7)$$

The calculated V_{oc} values for each device are 0.97 V for 1800 rpm, 1.00 V for 1950 rpm, and 0.95 V for 2150 rpm, which exhibit similar trends to the measured V_{oc} values (Table 2). However, since this equation does not include resistance parameters, the calculated V_{oc} values do not perfectly match the measured values.

The perovskite solar cell with a band gap energy of 1.59 eV can achieve a FF of 0.904, which is the Shockley−Queisser limit for FF. We calculated the theoretical FF, considering nonradiative loss and charge transport loss, using parameters extracted from the dark J−V curves and the following eqs (Figure 4d)[19,71]

$$FF_{max} = \frac{v_{oc} - \ln(v_{oc} + 0.72)}{v_{oc}} \text{ with } v_{oc} = \frac{qV_{oc}}{n_{id}k_BT} \quad (8)$$

$$FF_s = FF_{max}(1 - 1.1r_s) + \frac{r_s^2}{5.4} \text{ with } r_s = \frac{J_{sc}R_s}{V_{oc}} \quad (9)$$

and

$$FF = FF_s\left(1 - \frac{v_{oc} + 0.72}{v_{oc}}\frac{FF_s}{r_{sh}}\right) \text{ with } r_{sh} = \frac{J_{sc}R_{sh}}{V_{oc}} \quad (10)$$

The FF$_{max}$ values with neglected charge transport losses were 0.845, 0.853, and 0.813 for 1800, 1950, and 2150 rpm devices, respectively (Table 3), indicating that excess-PbI$_2$ and excess-FAI induced nonradiative recombination. The FF values, considering both nonradiative recombination and charge

Table 3. Measured and Calculated Fill Factor of the 1800, 1950, and 2150 rpm Devices by Using eqs 8, 9, and 10

devices	FF$_{max}$	calc. FF	meas. FF
1800 rpm	0.845	0.828	0.765
1950 rpm	0.853	0.832	0.776
2150 rpm	0.813	0.796	0.739

transport recombination loss, were 0.828, 0.832, and 0.796 for the 1800, 1950, and 2150 rpm devices, respectively. The calculated FF values showed a similar tendency to the measured FF, revealing that excess-PbI$_2$ and excess-FAI induced nonradiative recombination.

Compared to the 1950 rpm device, the 1800 rpm device had similar R_s and R_{sh}, and high n_{id} and J_0. Changes in these parameters suggest that excess-PbI$_2$ induces trap-assisted recombination, degrading V_{oc} and J_{sc} of the photovoltaic device (Figure 4e). On the other hand, the 2150 rpm device had a small R_{sh}, high n_{id}, and a high J_0. Excess-FAI not only induces trap-assisted recombination like excess-PbI$_2$ but also impedes charge transport to the charge transport layer, resulting in a leakage current. This increases charge accumulation at interfaces, induces hysteresis, and decreases light stability. It demonstrates that excess-FAI significantly degrades the V_{oc} and J_{sc} of PSCs and shows a broad distribution of photovoltaic parameters.

Furthermore, we calculated the PCE of each device using the calculated V_{oc}, J_{sc}, and FF without estimating photo J−V curves and compared these calculated values with the measured values (Table 4). The calculated PCE values for the 1800, 1950, and

Table 4. Calculated Photovoltaic Parameters and Measured PCE of the 1800, 1950, and 2150 rpm Devices

devices	calc. V_{oc} (V)	EQE. J_{sc} (mA/cm^2)	calc. FF	calc. PCE (%)	meas. PCE (%)
1800 rpm	0.97	23.42	0.828	18.80	18.12
1950 rpm	1.00	23.58	0.832	19.61	19.16
2150 rpm	0.95	23.21	0.796	17.54	16.05

2150 rpm devices were 18.80, 19.61, and 17.54%, respectively. When compared to the measured PCE values, we observed a small discrepancy, with errors of 3.62, 2.29, and 8.49% for the 1800, 1950, and 2150 rpm devices, respectively. Through numerical modeling, we can efficiently predict carrier recombination dynamics and device performance using a dark J−V curve of device.

2.4. Machine Learning Analysis of the Perovskite Solar Cells. While numerical modeling provides a valuable tool for predicting and optimizing photovoltaic device performance, its application is not without challenges. This method often demands the use of complex equations and may not accurately predict the performance of devices yet to be fabricated. As an alternative, machine learning models offer the potential to simplify this process, using existing data and experimental variables to predict unknown data, thereby
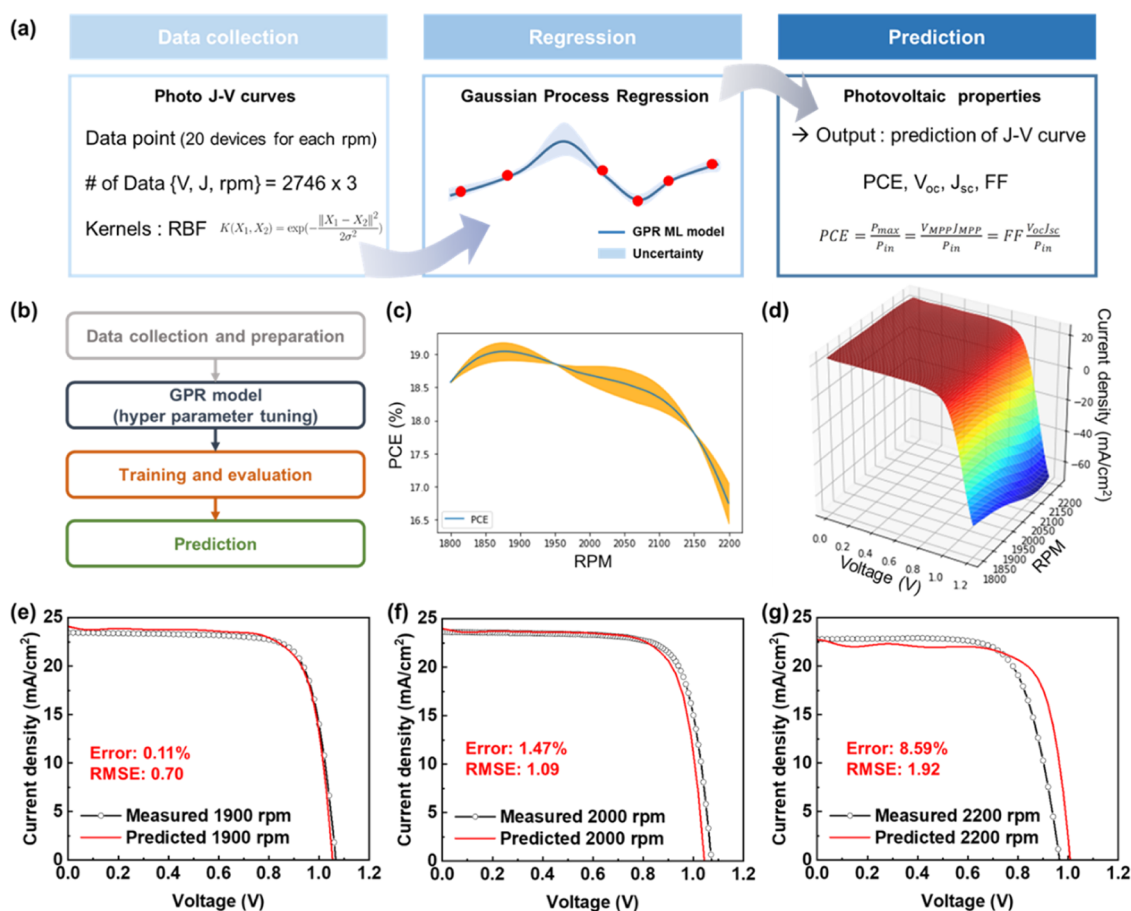
Figure 5. (a) Illustration of the machine learning model training process for device performance prediction. (b) Work flow of photo $J-V$ curve prediction using the machine learning model. (c) Predicted PCE and (d) predicted $J-V$ curves with various rpm by machine learning. (e−g) Comparison of predicted and fabricated device's photo $J-V$ curves measured under 1 sun illumination.

circumventing the need for intricate equations such as the Shockley diode equation. To further enhance our analytical approach, we have implemented a machine learning model to predict the photo $J-V$ curve, allowing us to efficiently anticipate the performance of untested devices without the necessity of complex equation fitting.

Our methodology, as depicted in the flowchart (Figure 5a,5b), involves predicting the device's $J-V$ curve as a function of the spin speed (rpm). We utilized photo $J-V$ curves of devices operating at 1800, 1950, and 2150 rpm to train our machine learning model. These curves, measured in 0.02 steps from −0.1 to 1.2 V, were collected from 20 devices varying in rpm. We trained the machine learning model using the Linear Regression, Random Forest, Support Vector Machine, Neural Network, Decision Tree, and Gaussian Process Regression (GPR) algorithm and evaluated their accuracy (Figure S6). Among them, the GPR algorithm was selected for the machine learning training because this algorithm is adept at managing small data sets and excels at resolving complex regression problems, including high-dimensional and nonlinear predictions.[72]

During the training phase focused on identifying the maximum power point (P_{max}), we found that the Linear and SVM algorithms did not fit the model well. Conversely, the Random Forest and Decision Tree algorithms demonstrated higher R^2 values compared with the GPR model. However, upon conducting performance predictions for perovskite solar

cells using these algorithms, we encountered limitations due to our relatively small data set and large data intervals. Specifically, the Random Forest and Decision Tree algorithms yielded inaccurate predictions under these conditions. As a result, we chose to continue using the GPR algorithm, as it is better suited for training models with smaller data sets and provides an uncertainty measure for predictions. It not only offers predicted values but also assesses the uncertainty of these predictions. Given the bell-shaped nature of GPR, this approach is particularly suitable for identifying maximum points.[73] GPR offers uncertainty quantification, providing an extra layer of reliability in predictions, and is particularly efficient at making accurate predictions even when the available data set is small or includes noise. We selected the radial basis function kernel, a generalized form of kernelization for the Gaussian distribution, for our analysis.

During the model evaluation phase, we calculated the root-mean-square error (RMSE) and the coefficient of determination (R^2) values to assess the performance using the training and testing data sets. The results are summarized in Table 5, with the RMSE calculated as

$$\text{RMSE} = \sqrt{\frac{1}{n} \sum_{i=1}^{n} (\hat{y}_i - y_i)^2}$$

(11)

and the R^2 calculated as

Table 5. Computed Trained and Tested R^2 and RMSE Value of the Machine Learning Model

devices	train_R^2	train_RMSE	test_R^2	test_RMSE
1800 rpm	0.9798	2.57	0.9627	3.31
1950 rpm	0.9692	2.95	0.9608	3.35
2150 rpm	0.9504	8.14	0.8936	8.40

$$R^2 = 1 - \frac{\sum_{i=1}^{n} (\hat{y}_i - y_i)^2}{\sum_{i=1}^{n} (\bar{y}_i - y_i)^2} \tag{12}$$

where n is the number of instances in the data set, $\hat{y}_i$ represents the measured value of the instance, y_i is the true value, and $\bar{y}_i$ is the mean value of y_i.

RMSE is sensitive to both small and large errors, with smaller values indicating a better fit.[74] The trained model yielded RMSE values of 2.57, 2.95, and 8.14, and the computed tested RMSE values were 3.31, 3.35, and 8.40 for the devices operating at 1800, 1950, and 2150 rpm, respectively (Figure S7). The relatively high RMSE value of our model may be attributed to the broad data distribution between 1.0 and 1.2 V (Figure S3).

The R^2 value provides another performance metric, with values closer to 1 indicating better regression fitting.[74,75] Generally, values above 0.8 are considered to be indicative of good fitting. The R^2 values obtained from the trained model were 0.9798, 0.9692, and 0.9504, and the tested R^2 values was 0.9627, 0.9608, and 0.8936 for the devices operating at 1800, 1950, and 2150 rpm, respectively. This level of accuracy is sufficient to consider the model as predictive and suggests that it also performs well on new data.[75]

Leveraging the trained two-dimensional (2D) GPR model, we were able to predict the power conversion efficiency (PCE) of the device (Figure 5c) by identifying the maximum point of the product of current density and voltage from the predicted photo $J-V$ curves as a function of the PbI_2 spin speed (rpm) (Figure 5d). The blue line in Figure 5c represents the predicted value, while the orange range denotes the 95% confidence region of the predicted value. According to the machine learning model, a device fabricated with a PbI_2 layer processed at 1870 rpm is anticipated to exhibit an optimal performance. In addition, we fabricated devices at 50 rpm intervals within the range of 1750−2200 rpm and obtained J−V curves to further validate the accuracy of the machine learning model (Figures S9 and S10). The predictions from the machine learning model trained with three points (1850, 1950, and 2150 rpm) were similar to those from the model trained at 50 rpm intervals, indicating that our machine learning model can efficiently predict device performance with a small amount of training data and narrow intervals.

In order to assess the accuracy of the machine learning model's predictions, we extracted the photo $J-V$ curves from the predicted data at 1900, 2000, and 2200 rpm. These were then compared with the photo $J-V$ curve from the actual device (Figure 5e−g). The difference between the measured and predicted PCE for the 1900 and 2000 rpm devices was 0.11 and 1.47%, respectively, with corresponding RMSE values of 0.70 and 1.09. The predicted $J-V$ curve for the 2200 rpm device, which falls outside the data range, showed an error of 8.59% and an RMSE of 1.92. This indicates that the machine learning model can effectively predict the performance of unexplored devices with minimal error within the range of the training data. However, when these predictions extend beyond the range of training data, they become substantially less accurate. By broadening the scope of the training data and increasing the number of data points, we anticipate an improvement in the predictive accuracy of the model.

Ultimately, the machine learning model forecasted a maximum PCE of 19.52% with V_{oc} of 1.07 V, J_{sc} of 23.59 mA/cm², and FF of 0.773 at a spin rate of 1870 rpm (Figure S11). These predictions were then experimentally verified with a fabricated device, which exhibited a PCE of 19.63% with a V_{oc} of 1.07 V, a J_{sc} of 23.88 mA/cm², and a FF of 0.768. These results suggest that the machine learning models employing Gaussian Process Regression provide efficient tools for predicting device performance and optimizing design parameters. This makes them particularly valuable in the context of multiple experiments concerning next-generation optoelectronic devices.

3. CONCLUSIONS

In summary, we fabricated and analyzed perovskite films at 1800 rpm (Ex-PbI_2), 1950 rpm (Optimized), and 2150 rpm (Ex-FAI) to optimize sequentially processed perovskite solar cells. To streamline the optimization process, we employed numerical modeling and machine learning techniques. These models can efficiently predict device performance using a single data type. Numerical modeling provides parameters that reveal carrier recombination dynamics in the devices, while the machine learning model can predict the $J-V$ curves of previously unexplored RPM without the need for complex equation fitting. This study presents a simple and efficient approach for optimizing and predicting the performance of next-generation photovoltaic devices.

4. MATERIALS AND METHODS

4.1. Materials. SnO_2 (15% H_2O colloidal dispersion) was purchased from Alfa Aesar. PbI_2 (99.99%) was purchased from TCI. FAI and MABr were purchased from GreatCell Solar. Spiro-OMeTAD was purchased from the Luminescence Technology Co. DMF (99.8%), DMSO (99.9%), 2-propanol (IPA, 99.5%), MACl (99.8%), bis(trifluoromethane)-sulfonimide lithium salt (Li-TFSI), and 4-*tert*-butylpyridine (TBP, 99.8%) were purchased from Sigma-Aldrich.

4.2. Device Fabrication. Indium-doped SnO_2 (ITO) conductive substrates were cleaned by using deionized water, acetone, and IPA. The cleaned substrate was then treated with UV−ozone for 20 min. For the electron transport layer (ETL), a SnO_2 colloidal solution diluted with deionized water (1:4 v/v %) was spin-coated at 3000 rpm for 30 s on the UV-treated substrate and then annealed at 180 °C for 30 min. The cells were then treated with ultraviolet (UV) ozone for 10 min. The perovskite layer was fabricated by sequential deposition. The PbI_2 precursor solution was prepared by mixing 691.5 mg of PbI_2, 0.95 mL of DMF, and 0.05 mL of DMSO. An organic salt solution was prepared as FAI/MABr/MACl (90/9/9 mg) in 1 mL IPA. The PbI_2 solution was deposited on the SnO_2 layer at 1800, 1950, and 2150 rpm for 30 s and then annealed at 70 °C for 1 min under inert conditions. An organic salt solution was deposited on the PbI_2 layer at 2000 rpm for 30 s and then annealed at 150 °C for 25 min. The hole-transporting layer (HTL) was spin-coated at 4000 rpm for 30 s on the perovskite layer using a solution of 72.3 mg of Spiro-OMeTAD, 28.8 μL of TBP, and 17.5 μL of Li-TFSI stock solution (520 mg of Li-TFSI in 1 mL of acetonitrile) in 1 mL of CB. An Au metal

contact with a thickness of 60 nm was deposited by thermal evaporation.

4.3. Characterization of Devices. To determine the structure and analyze the composition of the perovskite films, X-ray diffraction (XRD) spectra were obtained. Time-of-flight secondary ion mass spectrometry (TOF-SIMS) experiments were performed with a TOF-SIMS 5 (ION-TOF GmbH, Münster, Germany) at the KBSI Busan Center using a pulsed 30 keV Bi_1^+ primary beam with a current of 1.02 pA. The analyzed area used in this work is a square of 300 μm × 300 μm, and the data acquisition time is about 1638.40 s. Negative ion spectra were internally calibrated by using H^-, C^-, C_2^-, C_3^-, and C_4^- normalized to the respective secondary total ion yields. During data acquisition, chemical images of the analyzed area were captured with a 128 × 128 pixel resolution. Field emission-SEM (FE-SEM) (S-4700, Hitachi) images, Mott−Schottky spectra, and External quantum efficiency (EQE) spectra were obtained at the Future Energy Convergence Core Center (FECC) at Jeonbuk National University. To evaluate the photovoltaic performance of the device, photocurrent density−voltage ($J–V$) curves were measured with a voltage source meter (Keithley 4200) under AM 1.5G illumination (100 mA cm^{-2}) using a 1 kW Oriel solar simulator (with respect to a reference silicon photodiode calibrated with NREL). Atomic force microscopy (AFM, Multimode-8, and BRUKER) was conducted to confirm the roughness of the perovskite film installed at the Centre for University-wide Research Facilities (CURF) at Jeonbuk National University.

■ ASSOCIATED CONTENT

Ⓢ Supporting Information

The Supporting Information is available free of charge at https://pubs.acs.org/doi/10.1021/acsomega.3c05622.

AFM; XRD; photovoltaic statistics; Bode plots; trained data of $J−V$ curves; and optimized $J−V$ curve (PDF)

■ AUTHOR INFORMATION

Corresponding Author

Min Kim − *Graduate School of Integrated Energy-AI, Jeonbuk National University, Jeonju 54896, Republic of Korea; School of Chemical Engineering, Clean Energy Research Center, Jeonbuk National University, Jeonju 54896, Republic of Korea;* ⓞ orcid.org/0000-0002-9212-5673; Email: minkim@jbnu.ac.kr

Authors

Jeongbeom Cha − *Graduate School of Integrated Energy-AI, Jeonbuk National University, Jeonju 54896, Republic of Korea*

Dohun Baek − *School of Chemical Engineering, Clean Energy Research Center, Jeonbuk National University, Jeonju 54896, Republic of Korea*

Haedam Jin − *Graduate School of Integrated Energy-AI, Jeonbuk National University, Jeonju 54896, Republic of Korea*

Hyemi Na − *School of Chemical Engineering, Clean Energy Research Center, Jeonbuk National University, Jeonju 54896, Republic of Korea*

Geon Yeong Park − *School of Chemical Engineering, Clean Energy Research Center, Jeonbuk National University, Jeonju 54896, Republic of Korea; Chemical Materials Solutions*

Center, Korea Research Institute of Chemical Technology (KRICT), Daejeon 34114, Republic of Korea

Dong Seok Ham − *Chemical Materials Solutions Center, Korea Research Institute of Chemical Technology (KRICT), Daejeon 34114, Republic of Korea;* ⓞ orcid.org/0000-0002-8574-373X

Complete contact information is available at:
https://pubs.acs.org/10.1021/acsomega.3c05622

Author Contributions

All authors have given approval to the final version of the manuscript. J.C.: conceptualization, methodology, formal analysis, investigation, validation, writing−original draft. D.B.: conceptualization, methodology, formal analysis, investigation, validation, writing−original draft. H.J.: conceptualization, formal analysis, writing−original draft, writing−review and editing. H.N.: data curation, formal analysis, visualization. G.Y.P.: data curation, formal analysis, visualization. D.S.H.: writing−review and editing. M.K.: project administration, supervision, writing−review and editing.

Notes

The authors declare no competing financial interest.
Any additional relevant notes should be placed here.

■ ACKNOWLEDGMENTS

■ REFERENCES

(1) Yoo, J. J.; Shin, S. S.; Seo, J. Toward Efficient Perovskite Solar Cells: Progress, Strategies, and Perspectives. *ACS Energy Lett.* **2022**, 7, 2084−2091.

(2) Park, N.-G. Perovskite solar cells: an emerging photovoltaic technology. *Mater. Today* **2015**, 18 (2), 65−72.

(3) Jung, H. S.; Park, N. G. Perovskite solar cells: from materials to devices. *Small* **2015**, 11 (1), 10−25.

(4) Wang, M.; Feng, Y.; Bian, J.; Liu, H.; Shi, Y. A comparative study of one-step and two-step approaches for MAPbI3 perovskite layer and its influence on the performance of mesoscopic perovskite solar cell. *Chem. Phys. Lett.* **2018**, 692, 44−49.

(5) Im, J.-H.; Kim, H.-S.; Park, N.-G. Morphology-photovoltaic property correlation in perovskite solar cells: One-step versus two-step deposition of CH3NH3PbI3. *APL Mater.* **2014**, 2 (8), No. 081510.

(6) Prat, D.; Hayler, J.; Wells, A. A survey of solvent selection guides. *Green Chem.* **2014**, 16 (10), 4546−4551.

(7) Huang, H.; Shi, J.; Zhu, L.; Li, D.; Luo, Y.; Meng, Q. Two-step ultrasonic spray deposition of CH3NH3PbI3 for efficient and large-area perovskite solar cell. *Nano Energy* **2016**, 27, 352−358.

(8) Gong, C.; Tong, S.; Huang, K.; Li, H.; Huang, H.; Zhang, J.; Yang, J. Flexible Planar Heterojunction Perovskite Solar Cells Fabricated via Sequential Roll-to-Roll Microgravure Printing and Slot-Die Coating Deposition. *Sol. RRL* **2020**, 4 (2), No. 1900204, DOI: 10.1002/solr.201900204.

(9) Kim, Y. Y.; Park, E. Y.; Yang, T.-Y.; Noh, J. H.; Shin, T. J.; Jeon, N. J.; Seo, J. Fast two-step deposition of perovskite via mediator

extraction treatment for large-area, high-performance perovskite solar cells. *J. Mater. Chem. A* **2018**, 6 (26), 12447−12454.

(10) Yang, T.-Y.; Kim, Y. Y.; Seo, J. Roll-to-roll manufacturing toward lab-to-fab-translation of perovskite solar cells. *APL Mater.* **2021**, 9 (11), No. 110901.

(11) Liu, F.; Dong, Q.; Wong, M. K.; Djurišić, A. B.; Ng, A.; Ren, Z.; Shen, Q.; Surya, C.; Chan, W. K.; Wang, J. Is excess PbI2 beneficial for perovskite solar cell performance? *Adv. Energy Mater.* **2016**, 6 (7), No. 1502206.

(12) Jia, Y. H.; Neutzner, S.; Zhou, Y.; Yang, M.; Tapia, J. M. F.; Li, N.; Yu, H.; Cao, J.; Wang, J. P.; Petrozza, A.; et al. Role of Excess FAI in Formation of High-Efficiency FAPbI3-Based Light-Emitting Diodes. *Adv. Funct. Mater.* **2020**, 30 (1), No. 1906875.

(13) Hu, Z.; An, Q.; Xiang, H.; Aigouy, L.; Sun, B.; Vaynzof, Y.; Chen, Z. Enhancing the efficiency and stability of triple-cation perovskite solar cells by eliminating excess PbI2 from the perovskite/hole transport layer interface. *ACS Appl. Mater. Interfaces* **2020**, 12 (49), 54824−54832.

(14) Jiang, Q.; Chu, Z.; Wang, P.; Yang, X.; Liu, H.; Wang, Y.; Yin, Z.; Wu, J.; Zhang, X.; You, J. Planar-structure perovskite solar cells with efficiency beyond 21%. *Adv. Mater.* **2017**, 29 (46), No. 1703852.

(15) Emara, J.; Schnier, T.; Pourdavoud, N.; Riedl, T.; Meerholz, K.; Olthof, S. Impact of film stoichiometry on the ionization energy and electronic structure of CH3NH3PbI3 perovskites. *Adv. Mater.* **2016**, 28 (3), 553−559.

(16) Zhao, Z.; Cao, H.; Li, J.; Zhu, H.; Yang, L.; Yin, S. Strategies to obtain stoichiometric perovskite by sequential vapor deposition learned by modeling the diffusion-dominated formation of perovskite films. *Appl. Phys. Express* **2018**, 11 (10), No. 105501.

(17) Zhang, B.; Zhang, M. J.; Pang, S. P.; Huang, C. S.; Zhou, Z. M.; Wang, D.; Wang, N.; Cui, G. L. Carrier transport in CH3NH3PbI3 films with different thickness for perovskite solar cells. *Adv. Mater. Interfaces* **2016**, 3 (17), No. 1600327.

(18) Ali, A.; Cha, M. J.; Kang, H. I.; Park, Y. J.; Seo, J. H.; Walker, B. Influence of Film Thickness on the Electronic Band Structure and Optical Properties of P−I−N CH3NH3PbI3− xClx Perovskite Solar Cells. *Adv. Eng. Mater.* **2020**, 22 (7), No. 2000185.

(19) Cao, Q.; Li, Y.; Zhang, H.; Yang, J.; Han, J.; Xu, T.; Wang, S.; Wang, Z.; Gao, B.; Zhao, J.; et al. Efficient and stable inverted perovskite solar cells with very high fill factors via incorporation of star-shaped polymer. *Sci. Adv.* **2021**, 7 (28), No. eabg0633.

(20) Wang, Y.; Sun, Y.-Y.; Zhang, S.; Lu, T.-M.; Shi, J. Band gap engineering of a soft inorganic compound PbI2 by incommensurate van der Waals epitaxy. *Appl. Phys. Lett.* **2016**, 108 (1), No. 013105.

(21) Lifshitz, E.; Bykov, L.; Yassen, M.; Chen-Esterlit, Z. The investigation of donor and acceptor states in nanoparticles of the layered semiconductor PbI2. *Chem. Phys. Lett.* **1997**, 273 (5−6), 381−388.

(22) Sengupta, A.; Jiang, B.; Mandal, K.; Zhang, J. Ultrafast electronic relaxation dynamics in PbI2 semiconductor colloidal nanoparticles: a femtosecond transient absorption study. *J. Phys. Chem. B* **1999**, 103 (16), 3128−3137.

(23) Manoel, E.; Custódio, M.; Guimarães, F.; Bianchi, R. F.; Hernandes, A. C. Growth and characterization of HgI2, PbI2 and PbI2: HgI2 layered semiconductors. *Mater. Res.* **1999**, 2, 75−79.

(24) Birkhold, S. T.; Precht, J. T.; Giridharagopal, R.; Eperon, G. E.; Schmidt-Mende, L.; Ginger, D. S. Direct observation and quantitative analysis of mobile Frenkel defects in metal halide perovskites using scanning Kelvin probe microscopy. *J. Phys. Chem. C* **2018**, 122 (24), 12633−12639.

(25) Deng, Y.; Xu, S.; Chen, S.; Xiao, X.; Zhao, J.; Huang, J. Defect compensation in formamidinium−caesium perovskites for highly efficient solar mini-modules with improved photostability. *Nat. Energy* **2021**, 6 (6), 633−641.

(26) Tress, W.; Correa Baena, J. P.; Saliba, M.; Abate, A.; Graetzel, M. Inverted current−voltage hysteresis in mixed perovskite solar cells: polarization, energy barriers, and defect recombination. *Adv. Energy Mater.* **2016**, 6 (19), No. 1600396.

(27) Wu, F.; Pathak, R.; Chen, K.; Wang, G.; Bahrami, B.; Zhang, W.-H.; Qiao, Q. Inverted current−voltage hysteresis in perovskite solar cells. *ACS Energy Lett.* **2018**, 3 (10), 2457−2460.

(28) Chen, B.; Yang, M.; Priya, S.; Zhu, K. Origin of J−V hysteresis in perovskite solar cells. *J. Phys. Chem. Lett.* **2016**, 7 (5), 905−917.

(29) Bu, T.; Li, J.; Huang, W.; Mao, W.; Zheng, F.; Bi, P.; Hao, X.; Zhong, J.; Cheng, Y.-B.; Huang, F. Surface modification via self-assembling large cations for improved performance and modulated hysteresis of perovskite solar cells. *J. Mater. Chem. A* **2019**, 7 (12), 6793−6800.

(30) Rong, Y.; Hu, Y.; Ravishankar, S.; Liu, H.; Hou, X.; Sheng, Y.; Mei, A.; Wang, Q.; Li, D.; Xu, M.; et al. Tunable hysteresis effect for perovskite solar cells. *Energy Environ. Sci.* **2017**, 10 (11), 2383−2391.

(31) Zhao, P.; Kim, B. J.; Jung, H. S. Passivation in perovskite solar cells: A review. *Mater. Today Energy* **2018**, 7, 267−286.

(32) Chen, H.; Yan, H.; Cai, Y. Effects of Defect on Work Function and Energy Alignment of PbI2: Implications for Solar Cell Applications. *Chem. Mater.* **2022**, 34 (3), 1020−1029.

(33) Chen, Y.; Meng, Q.; Xiao, Y.; Zhang, X.; Sun, J.; Han, C. B.; Gao, H.; Zhang, Y.; Lu, Y.; Yan, H. Mechanism of PbI2 in Situ Passivated Perovskite Films for Enhancing the Performance of Perovskite Solar Cells. *ACS Appl. Mater. Interfaces* **2019**, 11 (47), 44101−44108.

(34) Meier, T.; Gujar, T. P.; Schönleber, A.; Olthof, S.; Meerholz, K.; van Smaalen, S.; Panzer, F.; Thelakkat, M.; Köhler, A. Impact of excess PbI2 on the structure and the temperature dependent optical properties of methylammonium lead iodide perovskites. *J. Mater. Chem. C* **2018**, 6 (28), 7512−7519.

(35) Yi, H.; Wang, D.; Duan, L.; Haque, F.; Xu, C.; Zhang, Y.; Conibeer, G.; Uddin, A. Solution-processed WO3 and water-free PEDOT: PSS composite for hole transport layer in conventional perovskite solar cell. *Electrochim. Acta* **2019**, 319, 349−358.

(36) Le Corre, V. M.; Duijnstee, E. A.; El Tambouli, O.; Ball, J. M.; Snaith, H. J.; Lim, J.; Koster, L. J. A. Revealing charge carrier mobility and defect densities in metal halide perovskites via space-charge-limited current measurements. *ACS Energy Lett.* **2021**, 6 (3), 1087−1094.

(37) Jacobsson, T. J.; Correa-Baena, J.-P.; Anaraki, E. H.; Philippe, B.; Stranks, S. D.; Bouduban, M. E.; Tress, W.; Schenk, K.; Teuscher, J.; Moser, J.-E.; et al. Unreacted PbI2 as a double-edged sword for enhancing the performance of perovskite solar cells. *J. Am. Chem. Soc.* **2016**, 138 (32), 10331−10343.

(38) Kapoor, V.; Bashir, A.; Haur, L. J.; Bruno, A.; Shukla, S.; Priyadarshi, A.; Mathews, N.; Mhaisalkar, S. Effect of Excess PbI2 in Fully Printable Carbon-based Perovskite Solar Cells. *Energy Technol.* **2017**, 5 (10), 1880−1886.

(39) Liu, C.; Zhang, D.; Li, Z.; Zhang, X.; Shen, L.; Guo, W. Efficient 4,4′,4″-tris(3-methylphenylphenylamino)triphenylamine (m-MTDATA) Hole Transport Layer in Perovskite Solar Cells Enabled by Using the Nonstoichiometric Precursors. *Adv. Funct. Mater.* **2018**, 28 (36), No. 1803126.

(40) von Hauff, E.; Klotz, D. Impedance spectroscopy for perovskite solar cells: characterisation, analysis, and diagnosis. *J. Mater. Chem. C* **2022**, 10 (2), 742−761.

(41) Li, M.; Yan, X.; Kang, Z.; Liao, X.; Li, Y.; Zheng, X.; Lin, P.; Meng, J.; Zhang, Y. Enhanced Efficiency and Stability of Perovskite Solar Cells via Anti-Solvent Treatment in Two-Step Deposition Method. *ACS Appl. Mater. Interfaces* **2017**, 9 (8), 7224−7231.

(42) Abdulrahim, S. M.; Ahmad, Z.; Mehmood, M. Q.; Paek, S.; Bhadra, J.; Al-Thani, N. J.; Nazeeruddin, M. K.; Belaidi, A.; Amani, M. Effect of illumination and applied potential on the electrochemical impedance spectra in triple cation (FA/MA/Cs) 3D and 2D/3D perovskite solar cells. *J. Electroanal. Chem.* **2021**, 902, No. 115800.

(43) Ebadi, F.; Taghavinia, N.; Mohammadpour, R.; Hagfeldt, A.; Tress, W. Origin of apparent light-enhanced and negative capacitance in perovskite solar cells. *Nat. Commun.* **2019**, 10 (1), No. 1574.

(44) Almora, O.; Aranda, C.; Mas-Marzá, E.; Garcia-Belmonte, G. On Mott-Schottky analysis interpretation of capacitance measure-

ments in organometal perovskite solar cells. *Appl. Phys. Lett.* **2016**, *109* (17), No. 173903.

(45) Chouhan, A. S.; Jasti, N. P.; Avasthi, S. Effect of interface defect density on performance of perovskite solar cell: Correlation of simulation and experiment. *Mater. Lett.* **2018**, *221*, 150−153.

(46) Fischer, M.; Tvingstedt, K.; Baumann, A.; Dyakonov, V. Doping profile in planar hybrid perovskite solar cells identifying mobile ions. *ACS Appl. Energy Mater.* **2018**, *1* (10), 5129−5134.

(47) Sandberg, O. J.; Kurpiers, J.; Stolterfoht, M.; Neher, D.; Meredith, P.; Shoaee, S.; Armin, A. On the Question of the Need for a Built-In Potential in Perovskite Solar Cells. *Adv. Mater. Interfaces* **2020**, *7* (10), No. 2000041.

(48) Syed, A. A.; Cai, L.; Zhu, F. High Built-in Potential Perovskite Solar Cells Realized by Incorporating a Hybrid Hole Extraction Layer. *Sol. RRL* **2020**, *4* (11), No. 2000393.

(49) Park, J. S.; Kim, G. U.; Lee, D.; Lee, S.; Ma, B.; Cho, S.; Kim, B. J. Importance of Optimal Crystallinity and Hole Mobility of BDT-Based Polymer Donor for Simultaneous Enhancements of Voc, Jsc, and FF in Efficient Nonfullerene Organic Solar Cells. *Adv. Funct. Mater.* **2020**, *30* (51), No. 2005787.

(50) Riedel, I.; Parisi, J.; Dyakonov, V.; Lutsen, L.; Vanderzande, D.; Hummelen, J. C. Effect of temperature and illumination on the electrical characteristics of polymer−fullerene bulk-heterojunction solar cells. *Adv. Funct. Mater.* **2004**, *14* (1), 38−44.

(51) Wang, Z.; Liu, X.; Jiang, H.; Zhou, X.; Zhang, L.; Pan, F.; Qiao, X.; Ma, D.; Ma, W.; Ding, L. Organic Solar Cells Based on High Hole Mobility Conjugated Polymer and Nonfullerene Acceptor with Comparable Bandgaps and Suitable Energy Level Offsets Showing Significant Suppression of Jsc−Voc Trade-Off. *Sol. RRL* **2019**, *3* (7), No. 1900079.

(52) Caprioglio, P.; Wolff, C. M.; Sandberg, O. J.; Armin, A.; Rech, B.; Albrecht, S.; Neher, D.; Stolterfoht, M. On the origin of the ideality factor in perovskite solar cells. *Adv. Energy Mater.* **2020**, *10* (27), No. 2000502.

(53) Tress, W.; Yavari, M.; Domanski, K.; Yadav, P.; Niesen, B.; Baena, J. P. C.; Hagfeldt, A.; Graetzel, M. Interpretation and evolution of open-circuit voltage, recombination, ideality factor and subgap defect states during reversible light-soaking and irreversible degradation of perovskite solar cells. *Energy Environ. Sci.* **2018**, *11* (1), 151−165.

(54) Calado, P.; Burkitt, D.; Yao, J.; Troughton, J.; Watson, T. M.; Carnie, M. J.; Telford, A. M.; O'Regan, B. C.; Nelson, J.; Barnes, P. R. Identifying dominant recombination mechanisms in perovskite solar cells by measuring the transient ideality factor. *Phys. Rev. Appl.* **2019**, *11* (4), No. 044005.

(55) Almora, O.; Cho, K. T.; Aghazada, S.; Zimmermann, I.; Matt, G. J.; Brabec, C. J.; Nazeeruddin, M. K.; Garcia-Belmonte, G. Discerning recombination mechanisms and ideality factors through impedance analysis of high-efficiency perovskite solar cells. *Nano Energy* **2018**, *48*, 63−72.

(56) Agarwal, S.; Seetharaman, M.; Kumawat, N. K.; Subbiah, A. S.; Sarkar, S. K.; Kabra, D.; Namboothiry, M. A.; Nair, P. R. On the uniqueness of ideality factor and voltage exponent of perovskite-based solar cells. *J. Phys. Chem. Lett.* **2014**, *5* (23), 4115−4121.

(57) Lee, J. H.; Cho, S.; Roy, A.; Jung, H.-T.; Heeger, A. J. Enhanced diode characteristics of organic solar cells using titanium suboxide electron transport layer. *Appl. Phys. Lett.* **2010**, *96* (16), No. 163303.

(58) Kirchartz, T.; Nelson, J. Device modelling of organic bulk heterojunction solar cells. *Multiscale Modell. Org. Hybrid Photovoltaics* **2014**, *352*, 279−324.

(59) Li, C.; Song, Z.; Zhao, D.; Xiao, C.; Subedi, B.; Shrestha, N.; Junda, M. M.; Wang, C.; Jiang, C. S.; Al-Jassim, M. Reducing saturation-current density to realize high-efficiency low-bandgap mixed tin−lead halide perovskite solar cells. *Adv. Energy Mater.* **2019**, *9* (3), No. 1803135.

(60) Cappelletti, M.; Casas, G.; Cedola, A. P.; y Blancá, E. P.; Soucase, B. M. Study of the reverse saturation current and series resistance of ppn perovskite solar cells using the single and double-diode models. *Superlattices Microstruct.* **2018**, *123*, 338−348.

(61) Kanoun, A.-A.; Kanoun, M. B.; Merad, A. E.; Goumri-Said, S. Toward development of high-performance perovskite solar cells based on CH3NH3GeI3 using computational approach. *Sol. Energy* **2019**, *182*, 237−244.

(62) Wang, Y.; Xiang, P.; Ren, A.; Lai, H.; Zhang, Z.; Xuan, Z.; Wan, Z.; Zhang, J.; Hao, X.; Wu, L.; et al. MXene-modulated electrode/SnO2 interface boosting charge transport in perovskite solar cells. *ACS Appl. Mater. Interfaces* **2020**, *12* (48), 53973−53983.

(63) Cojocaru, L.; Uchida, S.; Jayaweera, P. V.; Kaneko, S.; Nakazaki, J.; Kubo, T.; Segawa, H. Origin of the hysteresis in I−V curves for planar structure perovskite solar cells rationalized with a surface boundary-induced capacitance model. *Chem. Lett.* **2015**, *44* (12), 1750−1752.

(64) Bi, Z.; Zhang, S.; Thandapani, M.; Zhu, Y.; Zheng, Y.; Liem, N. Q.; Xiao, X.; Xu, G.; Guerrero, A.; Xu, X. High Shunt Resistance SnO2-PbO Electron Transport Layer for Perovskite Solar Cells Used in Low Lighting Applications. *Adv. Sustainable Syst.* **2021**, *5* (11), No. 2100120.

(65) Singh, R.; Sandhu, S.; Lee, J.-J. Elucidating the effect of shunt losses on the performance of mesoporous perovskite solar cells. *Sol. Energy* **2019**, *193*, 956−961.

(66) Wu, Y.; Yang, X.; Chen, H.; Zhang, K.; Qin, C.; Liu, J.; Peng, W.; Islam, A.; Bi, E.; Ye, F.; et al. Highly compact TiO2 layer for efficient hole-blocking in perovskite solar cells. *Appl. Phys. Express* **2014**, *7* (5), No. 052301.

(67) Proctor, C. M.; Nguyen, T.-Q. Effect of leakage current and shunt resistance on the light intensity dependence of organic solar cells. *Appl. Phys. Lett.* **2015**, *106* (8), No. 083301.

(68) Green, M. A. Accurate expressions for solar cell fill factors including series and shunt resistances. *Appl. Phys. Lett.* **2016**, *108* (8), No. 081111.

(69) Saleem, H.; Karmalkar, S. An analytical method to extract the physical parameters of a solar cell from four points on the illuminated $ J \{-\} V \$ curve. *IEEE Electron Device Lett.* **2009**, *30* (4), 349−352.

(70) Kumar, A.; Ranjan, P. Defects signature in VOC character-ization of thin-film solar cells. *Sol. Energy* **2021**, *220*, 35−42.

(71) Zeng, Y.; Li, D.; Xiao, Z.; Wu, H.; Chen, Z.; Hao, T.; Xiong, S.; Ma, Z.; Zhu, H.; Ding, L.; Bao, Q. Exploring the charge dynamics and energy loss in ternary organic solar cells with a fill factor exceeding 80%. *Adv. Energy Mater.* **2021**, *11* (31), No. 2101338.

(72) Ren, J.; Cai, J.; Li, J. High precision implicit function learning for forecasting supercapacitor state of health based on Gaussian process regression. *Sci. Rep.* **2021**, *11* (1), No. 12112.

(73) Pradhan, D. K.; Kumari, S.; Strelcov, E.; Pradhan, D. K.; Katiyar, R. S.; Kalinin, S. V.; Laanait, N.; Vasudevan, R. K. Reconstructing phase diagrams from local measurements via Gaussian processes: mapping the temperature-composition space to confidence. *npj Comput. Mater.* **2018**, *4*, No. 23, DOI: 10.1038/s41524-018-0078-7.

(74) Jiang, S.; Wu, C.-C.; Li, F.; Zhang, Y.-Q.; Zhang, Z.-H.; Zhang, Q.-H.; Chen, Z.-J.; Qu, B.; Xiao, L.-X.; Jiang, M.-L. Machine learning (ML)-assisted optimization doping of KI in MAPbI 3 solar cells. *Rare Met.* **2021**, *40*, 1698−1707.

(75) Liu, H.; Feng, J.; Dong, L. Quick screening stable double perovskite oxides for photovoltaic applications by machine learning. *Ceram. Int.* **2022**, *48* (13), 18074−18082.